Anomalous Hall conductivity of noncollinear magnetic antiperovskites

Gautam Gurung, Ding-Fu Shao,[*] Tula R. Paudel, and Evgeny Y. Tsymbal[†]

Department of Physics and Astronomy and Nebraska Center for Materials and Nanoscience, University of Nebraska,
Lincoln, Nebraska 68588-0299, USA

The anomalous Hall effect (AHE) is a well-known fundamental property of ferromagnetic metals, commonly associated with the presence of a net magnetization. Recently, an AHE has been discovered in noncollinear antiferromagnetic (AFM) metals. Driven by nonvanishing Berry curvature of AFM materials with certain magnetic space-group symmetry, anomalous Hall conductivity (AHC) is very sensitive to the specific type of magnetic ordering. Here, we investigate the appearance of AHC in antiperovskite materials family ANMn$_3$ ($A =$ Ga, Sn, Ni), where different types of noncollinear magnetic ordering can emerge. Using symmetry analyses and first-principles density-functional theory calculations, we show that with almost identical band structure the nearly degenerate noncollinear AFM Γ_{5g} and Γ_{4g} phases of GaNMn$_3$ have zero and finite AHC, respectively. In a noncollinear ferrimagnetic M-1 phase, GaNMn$_3$ exhibits a large AHC due to the presence of a sizable net magnetic moment. In the noncollinear antiperovskite magnets, transitions between different magnetic phases, exhibiting different AHC states, can be produced by doping, strain, or spin transfer torque, which makes these materials promising for novel spintronic applications.

I. INTRODUCTION

It is known that the anomalous Hall effect (AHE) emerges in metals with broken time-reversal symmetry and strong spin-orbit coupling (SOC) [1]. Usually, the AHE is found in ferromagnetic (FM) metals, where a transverse voltage generated by a longitudinal charge current is sensitive to the net magnetization. The intrinsic AHE is driven by a fictitious magnetic field in the momentum space associated with the Berry curvature, a quantity inherent in the electronic band structure [2]. With the magnitude and direction determined by the magnetization and SOC, this fictitious magnetic field controls the charge current in a similar way as a real magnetic field in the ordinary Hall effect. The AHE vanishes in conventional collinear antiferromagnetic (AFM) metals due to the anomalous Hall conductivities being opposite in sign and hence canceling each other for the two ferromagnetic sublattices with opposite magnetization. In other words, the existence of symmetry combining time reversal and lattice translation prohibits the AHE. This observation suggested that the presence of a nonvanishing net magnetic moment is the necessary condition to break the related symmetry and produce the AHE [3].

It appeared, however, that the AHE can be observed in certain types of noncollinear antiferromagnets, such as Mn$_3X$ alloys ($X =$ Ga, Ge, Ir, etc.) [4–8]. In these metals, the Mn moments are arranged in a Kagome-type lattice within the (111) plane. The magnetic space-group symmetry operations in these compounds cannot eliminate the total Berry curvature, leading to a nonvanishing AHE [4]. The presence of

a sizable AHE in noncollinear AFM metals is interesting for AFM spintronics, where an AFM order parameter, as a state variable, can be controlled on a much shorter time scale compared to magnetization in ferromagnets [9–11].

Importantly, specifics of magnetic ordering in noncollinear AFM materials associated with different magnetic space-group symmetries have a strong impact on the AHE [12,13]. For example, it was found that the AHC tensors have a different form in Mn$_3X$ ($X =$ Ga, Ge, and Sn) and Mn$_3Y$ ($Y =$ Rh, Ir, and Pt) compounds, due to different magnetic moment configurations. One can expect therefore that a significant change in the anomalous Hall conductivity (AHC) can emerge at the magnetic phase transition associated with switching between different noncollinear magnetic orderings. Realizing such an effect in practice would be interesting for potential spintronic applications, and therefore exploring the AHE in possible material systems with competing and tunable noncollinear magnetic phases is valuable.

Antiperovskite materials are potential candidates for the control of the AHE by tunable noncollinear magnetism. Antiperovskites have a perovskite structure, where cation and anion positions are interchanged [Fig. 1(a)]. Abundant functional properties have been discovered in these materials, such as superconductivity [14], magnetoresistance [15], and magnetovolume [16–18], magnetocaloric [19,20], and barocaloric [21] effects. Manganese nitride antiperovskites ANMn$_3$ ($A =$ Ga, Cu, Ni, etc.) are typically metallic and often reveal complex magnetic orderings [16,22,23]. Various magnetic phases, such as noncollinear AFM Γ_{5g} and Γ_{4g} phases and a noncollinear ferrimagnetic M-1 phase, have been found in these compounds (Fig. 1). Transformations between these magnetic phases can be induced by perturbations, such as doping, pressure, and temperature [23–25]. It has also been predicted that the transition between the Γ_{5g} and Γ_{4g} phases

---
[*]dfshao@unl.edu
[†]tsymbal@unl.edu
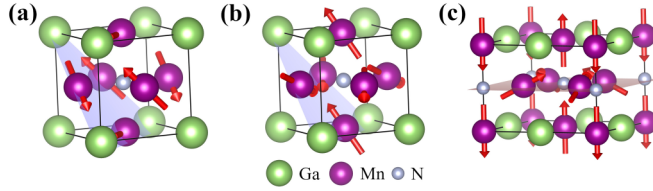
FIG. 1. Different noncollinear magnetic phases in AFM antiperovskite GaNMn$_3$: (a) Γ_{5g}, (b) Γ_{4g}, and (c) M-1. Red arrows denote magnetic moments.

TABLE I. Matrix elements of the AHC tensor for different magnetic phases in GaNMn$_3$. Here, the ordinary Cartesian coordinates are used, i.e., $\hat{x}||[100]$, $\hat{y}||[010]$, and $\hat{z}||[001]$.

Magnetic phase	Γ_{5g}	Γ_{4g}	M-1
Magnetic space group	$R\bar{3}m$	$R\bar{3}m'$	$P4$
AHC tensor	$\begin{bmatrix} 0 & 0 & 0 \\ 0 & 0 & 0 \\ 0 & 0 & 0 \end{bmatrix}$	$\begin{bmatrix} 0 & \sigma_{xy} & -\sigma_{xy} \\ -\sigma_{xy} & 0 & \sigma_{xy} \\ \sigma_{xy} & -\sigma_{xy} & 0 \end{bmatrix}$	$\begin{bmatrix} 0 & \sigma_{xy} & 0 \\ -\sigma_{xy} & 0 & 0 \\ 0 & 0 & 0 \end{bmatrix}$

can be achieved using a spin transfer torque [26]. These properties make ANMn$_3$ compounds promising for a functional control of the noncollinear magnetism and thus interesting for exploring the AHE in different magnetic phases.

In this paper, we consider gallium manganese nitride GaNMn$_3$ as a representative antiperovskite material to investigate the magnetic phase dependent AHC of the whole ANMn$_3$ family. The high-temperature paramagnetic phase of GaNMn$_3$ has a cubic crystal structure with the space group $Pm\bar{3}m$. The Γ_{5g} phase emerges below room temperature [Fig. 1(a)] and represents the most common noncollinear AFM phase of the ANMn$_3$ compounds. In this phase, to avoid the frustration from the triangular geometry of the Ga-Mn Kagome-type lattice in the (111) plane, the magnetic moments of the three Mn atoms form a chiral configuration with the 120° angle between each other. The Γ_{4g} magnetic structure is another common noncollinear AFM phase in the ANMn$_3$ family, which can be obtained from the Γ_{5g} phase by rotating all magnetic moments around the [111] axis by 90° [Fig. 1(b)]. Both the Γ_{5g} and Γ_{4g} phases have zero net magnetization. GaNMn$_3$ also exhibits a noncollinear ferrimagnetic M-1 phase [Fig. 1(c)], which can be stabilized by stoichiometric deficiency or high pressure [23]. In this phase, the Mn magnetic moments are antiferromagnetically (ferromagnetically) coupled in (between) the Ga-Mn (001) planes, resulting in collinear AFM sublattices within these planes. On the other hand, the magnetic moments in the Mn-N (002) planes are arranged noncollinearly [Fig. 1(c)], leading to the net magnetic moment along the [001] direction.

Using symmetry analyses and first-principles density-functional theory (DFT) calculations, we explore the AHE of the three noncollinear magnetic phases of GaNMn$_3$. We show that with nearly identical band structure the nearly degenerate AFM Γ_{5g} and Γ_{4g} phases have zero and finite AHC, respectively. A similar behavior is exhibited by noncollinear antiferromagnetic antiperovskites SnNMn$_3$ and NiNMn$_3$. In a noncollinear ferrimagnetic M-1 phase, GaNMn$_3$ exhibits a large AHC due to the presence of a sizeable net magnetization. With a possibility to control the appearance of these magnetic phases by external stimulus, the predicted variation of the AHC between different magnetic phases in the same material points to a useful approach of designing the AHE-based functional devices for spintronic applications.

II. SYMMETRY ANALYSIS

Within the linear response theory, the intrinsic AHC is expressed as the integral of the total Berry curvature ($\Omega_{\alpha\beta}$)

over the Brillouin zone (BZ) of the crystal [1,27]:

$$\sigma_{\alpha\beta} = -\frac{e^2}{\hbar} \int_{BZ} \frac{d^3\vec{k}}{(2\pi)^3} \Omega_{\alpha\beta}(\vec{k}), \quad (1)$$

where the total Berry curvature $\Omega_{\alpha\beta} = \sum_n f_n(\vec{k})\Omega_n^\gamma(\vec{k})$ is the sum of the Berry curvatures $\Omega_{n,\alpha\beta}(\vec{k})$ corresponding to the individual bands n, $f_n(\vec{k})$ is the Fermi distribution function, and indices (α, β) denote Cartesian coordinates. The expression for the Berry curvature $\Omega_{n,\alpha\beta}(\vec{k})$ is given by [1,27]

$$\Omega_{n,\alpha\beta}(\vec{k}) = -2i\hbar^2 \sum_{m\neq n} \frac{\langle \psi_{n,\vec{k}}|v_\alpha|\psi_{m,\vec{k}}\rangle \langle \psi_{m,\vec{k}}|v_\beta|\psi_{n,\vec{k}}\rangle}{[E_m(\vec{k}) - E_n(\vec{k})]^2}, \quad (2)$$

where $\psi_{n,\vec{k}}$ is the Bloch function and $\vec{v}$ is the velocity operator. Space-group symmetry of a material determines the presence or absence of a finite AHC. For example, since $\Omega_{n,\alpha\beta}(\vec{k})$ is odd with respect to time-reversal symmetry, i.e., $\Omega_{n,\alpha\beta}(-\vec{k}) = -\Omega_{n,\alpha\beta}(\vec{k})$, the total Berry curvature $\Omega_{\alpha\beta}$ and hence the AHC are zero for nonmagnetic materials. Similarly, if there is symmetry operation $\hat{O}$ transforming $\vec{k}$ to $\vec{k}'$ (i.e., $\vec{k}' = \hat{O}\vec{k}$), such as twofold rotation or mirror reflection, for which $\hat{O}\Omega_n(\vec{k}') = -\Omega_n(\vec{k})$, the AHC vanishes [12,13]. In noncollinear AFM materials, such as GaNMn$_3$, various magnetic phases are associated with different magnetic space-group symmetries (Table I), resulting in different AHC.

The Γ_{5g} phase of GaNMn$_3$ is characterized by a lattice of magnetic "whirls" composed of noncollinear Mn magnetic moments in the (111) plane [Fig. 2(a)]. This arrangement forms the magnetic space group $R\bar{3}m$, which has three mirror planes perpendicular to the (111) plane. Mirror symmetry M preserves the spin component perpendicular to the mirror plane and reverses the spin components parallel to the mirror plane. As shown in Fig. 2(a), the magnetic moments of the Mn atoms at the mirror planes [indicated by the dashed lines in Fig. 2(a)] are always perpendicular to this plane. Therefore, application of the symmetry transformations $M = M_{0\bar{1}1}$, $M_{10\bar{1}}$, or $M_{\bar{1}10}$ preserves the original configuration of magnetic moments. The invariance under these three mirror-symmetry transformations causes the AHE in the Γ_{5g} phase to vanish. For example, under the $M_{\bar{1}10}$ symmetry operation, the Berry curvature is transformed as $M_{\bar{1}10}\Omega_{xy}(k_y, k_x, k_z) = -\Omega_{xy}(k_x, k_y, k_z)$, which implies that the integral over the whole Brillouin zone in Eq. (1) leads to a zero σ_{xy}. Similarly, Ω_{yz} and Ω_{zx} are odd with respect to $M_{0\bar{1}1}$ and $M_{10\bar{1}}$, respec-

(a)
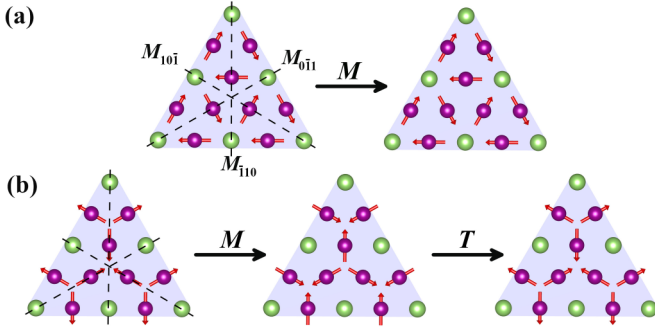
FIG. 2. Symmetry operations for noncollinear AFM phases Γ_{5g} (a) and Γ_{4g} (b) in the (111) Ga-Mn plane of GaNMn$_3$. (a) The Γ_{5g} phase preserves mirror planes ($\bar{1}10$), ($10\bar{1}$), and ($0\bar{1}1$) (denoted by dashed lines) and it is invariant under symmetry transformations $M = M_{0\bar{1}1}$, $M_{10\bar{1}}$, or $M_{\bar{1}10}$. (b) The Γ_{4g} phase does not preserve the mirror planes, but is invariant under the product of mirror symmetry M and time-reversal symmetry T. Red arrows denote the magnetic moments. Dotted lines denote the mirror planes.

tively. Table IV in Appendix B shows details of different symmetry transformations.

This odd property of the Berry curvature in GaNMn$_3$ under the mirror-symmetry transformations is broken in the Γ_{4g} phase. In this phase, the Mn magnetic moments form a lattice of "vertices" in the (111) plane, in which the magnetic moments of the Mn atoms within the mirror plane are parallel to this plane [Fig. 2(b)]. This configuration corresponds to the magnetic space group $R\bar{3}m'$, in which the mirror symmetries are broken. As seen from Fig. 2(b), mirror-symmetry transformation M reverses all the magnetic moments.

In contrast, the product of mirror symmetry M and time-reversal symmetry T is preserved in the Γ_{4g} phase. As shown in Fig. 2(b), when reversal of all moments by the mirror-symmetry operation M is followed by the time-reversal symmetry transformation T all the moments are reversed back to their initial configuration. The presence of the combined TM symmetry makes the Berry curvature an even function of wave vector $\vec{k}$. For example, applying the $TM_{\bar{1}10}$ transformation we obtain $TM_{\bar{1}10}\Omega_{xy}(k_y, k_x, k_z) = \Omega_{xy}(-k_x, -k_y, -k_z)$. This even property of the Berry curvature with respect to $TM_{\bar{1}10}$, $TM_{[0\bar{1}1]}$, and $TM_{[10\bar{1}]}$ makes the AHC nonzero in the Γ_{4g} phase. The complete analysis of the TM symmetry transformations is given in Table IV in Appendix B.

Magnetic space-group symmetry determines the shape of the AHC tensor. While in the Γ_{5g} phase, all the nine components of the AHC tensor are zero; in the Γ_{4g} phase, corresponding to the magnetic space group $R\bar{3}m'$, the AHC tensor is nonzero. Table I shows that there are six nonvanishing matrix elements of the AHC tensor in the Γ_{4g} phase with only one σ_{xy} being independent.

In the noncollinear ferrimagnetic M-1 phase, the unit cell is a tetragonal $\sqrt{2} \times \sqrt{2} \times 1$ supercell of the conventional cubic unit cell without any distortion [Fig. 1(c)]. In this phase, GaNMn$_3$ has a net magnetization along the [001] direction. Therefore, a nonzero AHC is expected in this case similar to that in ferromagnetic metals. Table I shows the AHC tensor for the magnetic space-group symmetry $P4$ corresponding to the

TABLE II. Calculated lattice parameters a and AHC σ_{xy} for different magnetic phases of ANMn$_3$ (A = Ga, Ni, Sn).

ANMn$_3$	a(Å)			σ_{xy} (Ω^{-1} cm^{-1})		
	Γ_{5g}	Γ_{4g}	M-1	Γ_{5g}	Γ_{4g}	M-1
GaNMn$_3$	3.87	3.87	3.82	0	40	377
NiNMn$_3$	3.84	3.84		0	130	
SnNMn$_3$	3.99	3.99		0	133	

M-1 phase. Like in collinear ferromagnetic metals, the AHC tensor has two nonzero components with only one σ_{xy} being independent.

III. METHODS

Next, we perform first-principles DFT calculations to obtain the AHC of the three noncollinear magnetic phases of GaNMn$_3$. The DFT calculations are performed using a plane-wave pseudopotential method with the fully relativistic ultrasoft pseudopotentials [28] implemented in QUANTUM-ESPRESSO [29]. The exchange and correlation effects are treated within the generalized gradient approximation [30]. We use the plane-wave cutoff energy of 52 Ry, the charge density cutoff energy of 520 Ry, and the k-point mesh of $16 \times 16 \times 16$ for the cubic Γ_{5g} and Γ_{4g} phases and $12 \times 12 \times 16$ for the tetragonal M-1 phase in GaNMn$_3$. Spin-orbit coupling is included in all the calculations. The electronic structure is converged to 10^{-7} eV/cell. The lattice parameters are obtained by fitting the calculated total energy to the Murnaghan equation of state [31].

The AHC is calculated using the PAOFLOW code [32] based on pseudoatomic orbitals [33,34]. Tight-binding Hamiltonians are constructed from the non-self-consistent DFT calculations with a $16 \times 16 \times 16$ k-point mesh for the Γ_{5g} and Γ_{4g} phases and a $12 \times 12 \times 16$ k-point mesh for the M-1 phase. Then, the AHC are calculated with a $48 \times 48 \times 48$ k-point mesh for the Γ_{5g} and Γ_{4g} phases and a $46 \times 46 \times 48$ k-point mesh for the M-1 phase using the adaptive broadening method. We find satisfactory convergence of the calculated AHC for a k mesh of denser than $40 \times 40 \times 40$. Increasing the grid size to $100 \times 100 \times 100$ changed the AHC negligibly.

The symmetry determined geometries of the AHC tensor are obtained using the FINDSYM code and the linear response symmetry code [35]. The figures are created using VESTA [36] and gnuplot [37].

IV. RESULTS

The calculated lattice parameters of GaNMn$_3$ in different magnetic phases are listed in Table II. For the Γ_{5g} phase of GaNMn$_3$, we find $a = 3.869$ Å, which is close to the experimental and previously calculated values [22,23,38–40] and is identical to the calculated lattice parameter of Γ_{4g}. The calculated lattice parameter of the M-1 phase is smaller, which is consistent with the emergence of the M-1 phase in GaNMn$_3$ under high pressure in experiment. We find that the Γ_{5g} phase is the ground state of GaNMn$_3$, while the total energies of the Γ_{4g} and M-1 phases are higher by 0.49 and
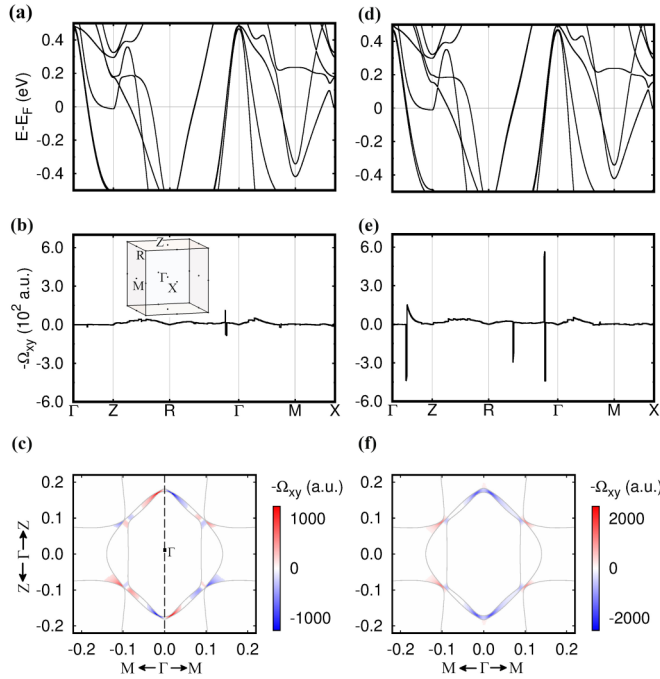
FIG. 3. (a)–(c) The calculated band structure (a), Berry curvature Ω_{xy} along the high-symmetry path (b), and the color map of Ω_{xy} in the $(\bar{1}10)$ plane (c) for the Γ_{5g} phase of GaNMn$_3$. (d)–(f) The calculated band structure (d), Ω_{xy} along the high-symmetry path (e), and the color map of Ω_{xy} in the $(\bar{1}10)$ plane (f) for the Γ_{4g} phase of GaNMn$_3$. The inset of (b) shows the Brillouin zone. The solid lines and the dashed line in (c) and (f) denote the Fermi surfaces and the mirror plane $M_{\bar{1}10}$.

164.35 meV/f.u., respectively. This result is consistent with the experimental observations showing the appearance of the Γ_{5g} phase in GaNMn$_3$ at low temperature [21,22,24].

The calculated local magnetic moment in the Γ_{5g} and Γ_{4g} phases is about $2.16 \mu_B$/Mn atom, which is in a qualitative agreement with the experimental and previously calculated values [22,23,38,39]. As expected, the noncollinear AFM configuration leads to a zero net magnetic moment. For the ferrimagnetic M-1 phase, we obtain $2.00 \mu_B$ per Mn atom in the (001) plane and $1.47 \mu_B$ per Mn atom in the (002) plane, resulting in the net magnetic moment of $1.80 \mu_B$/f.u pointing along the z direction.

Since Γ_{5g} and Γ_{4g} have similar magnetic structures, we first investigate the AHE in these two phases of GaNMn$_3$. Figure 3(a) shows the band structure of the Γ_{5g} phase. Five bands cross the Fermi energy (E_F). These dispersive bands are largely composed of the Mn-3d orbitals. It is seen that in some directions the bands are very close to each other. For example, along the Γ-Z and R-Γ directions, there are nearly degenerate bands.

Figure 3(b) shows the calculated Berry curvature Ω_{xy}. It is seen that there are peaks along the R-Γ direction, which appear, according to Eq. (2), due to the small band separation between the three bands crossing E_F along this direction close to the Γ point [see Fig. 3(a)]. Along the Γ-Z direction, the Berry curvature Ω_{xy} is zero within the computation accuracy. This is due to the mirror symmetry $M_{\bar{1}10}$ which holds along this

high-symmetry direction, resulting in $M_{\bar{1}10}\Omega_{xy}(0, 0, k_z) = -\Omega_{xy}(0, 0, k_z)$, and hence $\Omega_{xy}(0, 0, k_z) = 0$.

In order to demonstrate the odd nature of the Berry curvature under the mirror symmetry $M_{\bar{1}10}$, we plot in Fig. 3(c) the color map of Ω_{xy} around the Γ point in the (110) plane, which is perpendicular to the $(\bar{1}10)$ plane. It is seen that hot spots (i.e., regions where the absolute values of the Berry curvature are large) appear around the k points where the Fermi surfaces of different bands [indicated by solid lines in Fig. 3(c)] cross. As is evident from Fig. 3(c), Ω_{xy} changes sign with respect to the mirror-symmetry transformation $M_{\bar{1}10}$ [reflection with respect to the dashed line in Fig. 3(c)]. Clearly, integration of the Ω_{xy} over the whole Brillouin zone using Eq. (1) leads to zero AHC (within the computational accuracy) for the Γ_{5g} phase. As seen from Fig. 5(a), this property is independent of energy (Fermi energy).

Figure 3(d) shows the band structure of GaNMn$_3$ in the Γ_{4g} phase. The Γ_{4g} phase can be obtained from the Γ_{5g} phase by rotation of all magnetic moments around the [111] axis by 90°; in the absence of SOC the band structures of the two phases should be identical. Thus, the subtle differences in the band structures in Figs. 3(a) and 3(d) are due to SOC. These differences are seen, particularly, along the Γ-Z and Γ-R directions, where there is a slight increase in the band splitting around the Fermi energy.

Figure 3(e) shows the calculated Berry curvature of GaNMn$_3$ in the Γ_{4g} phase and reveals pronounced peaks in Ω_{xy} along the Γ-Z and Γ-R directions. According to the $TM_{\bar{1}10}$ symmetry, Ω_{xy} is an even function of the wave vector $\vec{k}$, i.e., $TM_{\bar{1}10}\Omega_{xy}(k_y, k_x, k_z) = \Omega_{xy}(-k_x, -k_y, -k_z)$. This is reflected in the calculated color map of Ω_{xy} around the Γ point in the (110) plane, which is shown in Fig. 3(f). It is seen that the hot spots of Ω_{xy} appear nearly at the same locations as for the Γ_{5g} phase [Fig. 3(c)]. However, in the Γ_{4g} phase, they are distributed symmetrically and have the same sign, proving that Ω_{xy} is an even function with respect the $TM_{\bar{1}10}$ symmetry transformation. The AHC is calculated by integration of Ω_{xy} according to Eq. (2). Figure 5(a) shows that σ_{xy} is finite as a function of energy and at the Fermi energy $\sigma_{xy} = -40$ Ω^{-1} cm^{-1}. Clearly, the difference in the AHC between the Γ_{5g} and Γ_{4g} phases is due to the different magnetic space-group symmetry of these phases.

Figure 4(a) shows the calculated band structure of GaNMn$_3$ in the M-1 phase along high-symmetry directions in the Brillouin zone. The band structure is more intricate compared to those for the Γ_{5g} and Γ_{4g} phases, because of a larger unit cell and more complex magnetic configuration. The presence on the net magnetic moment breaks time-reversal symmetry, which makes the AHC nonzero. Figure 5(b) shows the calculated Berry curvature Ω_{xy} along the high-symmetry directions. It is seen that there are number of pronounced broad peaks which are associated with the multiple low dispersive bands around the Fermi energy, which are coupled by the spin-orbit interaction. Figure 5(b) shows the calculated AHC as a function of energy in the M-1 phase. At the Fermi energy, $\sigma_{xy} = 377$ Ω^{-1} cm^{-1}, which is much larger than the AHC in the Γ_{4g} phase, due to the presence of the net magnetic moment in the M-1 phase. It is notable that σ_{xy} can be strongly enhanced in the M-1 phase by hole doping. For example, at
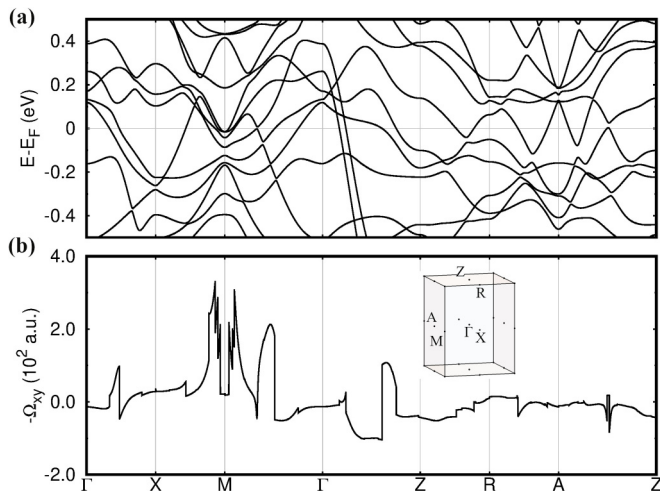
FIG. 4. Calculated band structure (a) and Berry curvature Ω_{xy} (b) of GaNMn$_3$ in the M-1 phase along high-symmetry paths in the Brillouin zone. The inset of (b) shows the Brillouin zone.

$E = E_F - 0.1$ eV, the calculated value of σ_{xy} is as large as 816 Ω^{-1} cm^{-1} which is larger than the AHC in Fe ($\sigma_{xy} \sim 700$ Ω^{-1} cm^{-1} [41]).

Similar properties are expected for other antiperovskite compounds, which may exhibit the noncollinear magnetic Γ_{4g} or Γ_{5g} phases. For comparison, we have calculated the AHC of antiperovskites NiNMn$_3$ and SnNMn$_3$, in which the Γ_{4g} phase exists at room temperature [16]. Consistent with the experiment, our calculations find that the Γ_{4g} phase is the ground state for these compounds. The calculated energy difference $\Delta E = E_{5g} - E_{4g}$ is 0.19 meV/f.u. for NiNMn$_3$ and 0.16 meV/f.u. for SnNMn$_3$. Large AHC over 100 Ω^{-1}cm^{-1} is predicted for the Γ_{4g} phase of NiNMn$_3$ and SnNMn$_3$, as indicated in Table II. The AHE in the Γ_{4g} phase of NiNMn$_3$ has been recently observed experimentally, which confirms our results [42]. Contrary to GaNMn$_3$, we find that the M-1 magnetic configuration is unstable in the NiNMn$_3$ and SnNMn$_3$ antiperovskites.
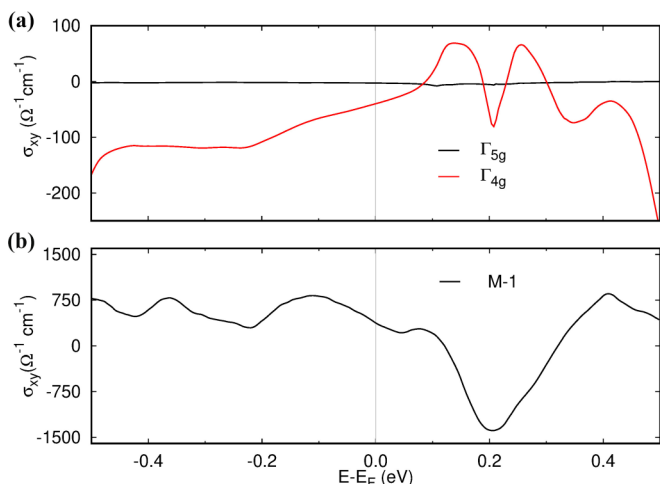
FIG. 5. (a), (b) Calculated AHC σ_{xy} as a function of energy for the Γ_{5g} and Γ_{4g} (a) and M-1 (b) phases of GaNMn$_3$.

V. DISCUSSION

Our results demonstrate that in the family of antiperovskite compounds, as represented by ANMn$_3$, the AHC is strongly dependent on the specific magnetic configuration. A significant change in the AHC can be produced by transitions between different magnetic phases. Such transitions can be driven by an external stimulus, provided that the energies of the different noncollinear magnetic phases are engineered to be nearly degenerate.

In experiment, the Γ_{5g} phase is found in the ANMn$_3$ compounds with $A =$ Zn, Ga; and the Γ_{4g} phase is found for $A =$ Ni, Ag, Sn [16]. The M-1 phase can be produced by nonstoichiometry and pressure [23]. These facts imply the sensitivity of the noncollinear magnetic phases to the chemical composition and lattice volume. Recently, monocrystalline ANMn$_3$ films have been successfully grown on different substrates, such as SrTiO$_3$, BaTiO$_3$, and LSAT [43,44]. This opens a possibility to engineer antiperovskite compounds with nearly degenerate energies of the different magnetic phases by proper doping and suitable epitaxial strain produced by the substrate. In particular, the dynamic strain generated by a piezoelectric substrate, such as PMN-PT, can be used to realize the reversible switching between different magnetic phases.

Furthermore, since the AHC is odd under time-reversal symmetry, the antiferromagnetic Γ_{4g} phase with a reversed Néel vector [corresponding to 180° rotation of all magnetic moments in the (111) plane] is expected to have AHC of opposite sign. The Néel vector can be switched using a spin transfer torque induced by a spin-polarized current [26], and its switching can be detected by the sign change of AHC. This functionality can be engineered by stoichiometry design of the antiperovskite compounds to tune the energy barrier between the two Γ_{4g} states of the opposite Néel vector ($\Delta E = E_{5g} - E_{4g}$) to a lower positive value. These possibilities make the ANMn$_3$ family of materials a promising platform for the AHE based applications of spintronic devices.

VI. SUMMARY

In this paper, we have studied the intrinsic AHC in different noncollinear magnetic phases of GaNMn$_3$, as a representative of a broader materials family of antiperovskite compounds ANMn$_3$ (A is a main group element). Based on the symmetry analysis and first-principles DFT calculations, we showed that the nearly degenerate noncollinear AFM Γ_{5g} and Γ_{4g} phases of GaNMn$_3$ have zero and finite AHC, respectively. This difference was explained by the different magnetic space-group symmetry of these phases. We also predicted that GaNMn$_3$, in the noncollinear ferrimagnetic M-1 phase, exhibits large AHC

TABLE III. AHC matrix tensors for Γ_{5g} and Γ_{4g} magnetic phases with $\hat{x}||[\bar{1}10]$, $\hat{y}||[\bar{1}\bar{1}2]$, and $\hat{z}||[111]$.

Magnetic phase	Γ_{5g}			Γ_{4g}		
AHC tensor	$\begin{bmatrix} 0 & 0 & 0 \\ 0 & 0 & 0 \\ 0 & 0 & 0 \end{bmatrix}$			$\begin{bmatrix} 0 & \sigma'_{xy} & 0 \\ -\sigma'_{xy} & 0 & 0 \\ 0 & 0 & 0 \end{bmatrix}$		

TABLE IV. Symmetry transformations of wave vector k and Berry curvature Ω.

	Transformation of k	Transformation of $\mathbf{\Omega}$
$\boldsymbol{M}_{[\bar{1}10]}$	$M_{[\bar{1}10]}(k_y, k_x, k_z) = (k_x, k_y, k_z)$	$M_{[\bar{1}10]}\Omega_{xy}(k_y, k_x, k_z) = -\Omega_{xy}(k_x, k_y, k_z)$ $M_{[\bar{1}10]}\Omega_{zx}(k_y, k_x, k_z) = -\Omega_{zy}(k_x, k_y, k_z)$ $M_{[\bar{1}10]}\Omega_{yz}(k_y, k_x, k_z) = -\Omega_{zx}(k_x, k_y, k_z)$
$\boldsymbol{M}_{[0\bar{1}1]}$	$M_{[0\bar{1}1]}(k_x, k_z, k_y) = (k_x, k_y, k_z)$	$M_{[0\bar{1}1]}\Omega_{xy}(k_x, k_z, k_y) = -\Omega_{zx}(k_x, k_y, k_z)$ $M_{[0\bar{1}1]}\Omega_{yz}(k_x, k_z, k_y) = -\Omega_{yz}(k_x, k_y, k_z)$ $M_{[0\bar{1}1]}\Omega_{zx}(k_x, k_z, k_y) = -\Omega_{xy}(k_x, k_y, k_z)$
$\boldsymbol{M}_{[10\bar{1}]}$	$M_{[10\bar{1}]}(k_z, k_y, k_x) = (k_x, k_y, k_z)$	$M_{[10\bar{1}]}\Omega_{xy}(k_z, k_y, k_x) = -\Omega_{zy}(k_x, k_y, k_z)$ $M_{[10\bar{1}]}\Omega_{yz}(k_z, k_y, k_x) = -\Omega_{xy}(k_x, k_y, k_z)$ $M_{[10\bar{1}]}\Omega_{zx}(k_z, k_y, k_x) = -\Omega_{zx}(k_x, k_y, k_z)$
$\boldsymbol{TM}_{\bar{1}10}$	$TM_{\bar{1}10}(k_y, k_x, k_z) = (-k_x, -k_y, -k_z)$	$TM_{[\bar{1}10]}\Omega_{xy}(k_y, k_x, k_z) = \Omega_{xy}(-k_x, -k_y, -k_z)$ $TM_{[\bar{1}10]}\Omega_{yz}(k_y, k_x, k_z) = \Omega_{zx}(-k_x, -k_y, -k_z)$ $TM_{[\bar{1}10]}\Omega_{zx}(k_y, k_x, k_z) = \Omega_{yz}(-k_x, -k_y, -k_z)$
$\boldsymbol{TM}_{[0\bar{1}1]}$	$TM_{[0\bar{1}1]}(k_x, k_z, k_y) = (-k_x, -k_y, -k_z)$	$TM_{[0\bar{1}1]}\Omega_{xy}(k_x, k_z, k_y) = \Omega_{zx}(-k_x, -k_y, -k_z)$ $TM_{[0\bar{1}1]}\Omega_{yz}(k_x, k_z, k_y) = \Omega_{yz}(-k_x, -k_y, -k_z)$ $TM_{[0\bar{1}1]}\Omega_{zx}(k_x, k_z, k_y) = \Omega_{xy}(-k_x, -k_y, -k_z)$
$\boldsymbol{TM}_{[10\bar{1}]}$	$TM_{[10\bar{1}]}(k_z, k_y, k_x) = (-k_x, -k_y, -k_z)$	$TM_{[10\bar{1}]}\Omega_{xy}(k_z, k_y, k_x) = \Omega_{yz}(-k_x, -k_y, -k_z)$ $TM_{[10\bar{1}]}\Omega_{yz}(k_z, k_y, k_x) = \Omega_{xy}(-k_x, -k_y, -k_z)$ $TM_{[10\bar{1}]}\Omega_{zx}(k_z, k_y, k_x) = \Omega_{zx}(-k_x, -k_y, -k_z)$

which is comparable to the AHC in elemental ferromagnets, such as iron, and calculated the AHC of antiperovskites SnNMn$_3$ and NiNMn$_3$ exhibiting the Γ_{4g} ground state. We argued that by doping and strain it is possible to engineer the ANMn$_3$ compounds where the energy difference between these magnetic phases could be small, so that an external stimulus, such as the dynamic strain or the spin transfer torque, could produce switchable magnetic phase transitions. Our paper demonstrates that the antiperovskite family of non-collinear magnetic materials is a good platform to realize the multiple AHE states in a single compound, which is promising for novel spintronic applications.

Note added. After the submission of our paper, we became aware of two relevant works on the anomalous Hall effect in ANMn$_3$ compounds [42,45].

ACKNOWLEDGMENTS

APPENDIX A: GEOMETRY DEPENDENCE OF AHC

The AHC tensor depends on geometry used in transport measurements. Table I (Sec. II) above shows the AHC tensor for GaNMn$_3$ (001) growth orientation corresponding to the standard Cartesian coordinates with x along [100], y along [010], and z along [001] directions. For the GaNMn$_3$ (111) sample, the AHC can be measured for a charge current parallel to the Ga-Mn Kagome lattice. Here we show the AHC tensor for a GaNMn$_3$ (111) sample, with x pointing along [$\bar{1}$10], y along [$\bar{1}\bar{1}$2], and z along [111] directions. The respective AHC tensor $\sigma_{[111]}$ can be obtained from

$$\sigma_{[111]} = R\,\sigma_{[001]}\,R^{-1}, \tag{A1}$$

where $\sigma_{[001]}$ is the AHC tensor for GaNMn$_3$ (001) and R represents the respective rotation matrix. The resulting AHC tensors for Γ_{4g} and Γ_{5g} phases are shown in Table III, where $\sigma'_{xy} = -68\ \Omega^{-1}\ \mathrm{cm}^{-1}$.

APPENDIX B: M AND TM SYMMETRY OPERATIONS ON THE BERRY CURVATURE

Table IV shows details of different symmetry transformations.

[1] N. Nagaosa, J. Sinova, S. Onoda, A. H. MacDonald, and N. P. Ong, Anomalous Hall effect, Rev. Mod. Phys. **82**, 1539 (2010).

[2] D. Xiao, M.-C. Chang, and Q. Niu, Berry phase effects on electronic properties, Rev. Mod. Phys. **82**, 1959 (2010).

[3] Z. Fang, N. Nagosa, K. S. Takahashi, A. Asamitsu, R. Mathieu, T. Ogasawara, H. Yamada, M. Kawasaki, Y. Tokura, and K. Terakura, The anomalous Hall effect and magnetic monopoles in momentum space, Science **302**, 92 (2003).

[4] H. Chen, Q. Niu, and A. H. MacDonald, Anomalous Hall Effect Arising from Noncollinear Antiferromagnetism, Phys. Rev. Lett. **112**, 017205 (2014).

[5] J. Kübler and C. Felser, Non-collinear antiferromagnets and the anomalous Hall effect, Europhys. Lett. **108**, 67001 (2014).

[6] S. Nakatsuji, N. Kiyohara, and T. Higo, Large anomalous Hall effect in a non-collinear antiferromagnet at room temperature, Nature (London) **527**, 212 (2015).

[7] A. K. Nayak, J. E. Fischer, Y. Sun, B. Yan, J. Karel, A. C. Komarek, C. Shekhar, N. Kumar, W. Schnelle, J. Kübler, C. Felser, and S. P. P. Parkin, Large anomalous Hall effect driven by a nonvanishing Berry curvature in the noncollinear antiferromagnet Mn$_3$Ge, Sci. Adv. **2**, e1501870 (2016).

[8] Y. Zhang, Y. Sun, H. Yang, J. Železný, S. P. P. Parkin, C. Felser, and B. Yan, Strong anisotropic anomalous Hall effect and spin Hall effect in the chiral antiferromagnetic compounds Mn$_3$X (X = Ge, Sn, Ga, Ir, Rh, and Pt), Phys. Rev. B **95**, 075128 (2017).

[9] A. H. MacDonald and M. Tsoi, Antiferromagnetic metal spintronics, Phil. Trans. R. Soc. A **369**, 3098 (2011).

[10] T. Jungwirth, X. Marti, P. Wadley, and J. Wunderlich, Antiferromagnetic spintronics, Nat. Nano. **11**, 231 (2016).

[11] O. Gomonay, V. Baltz, A. Brataa, and Y. Tserkovnyak, Antiferromagnetic spin textures and dynamics, Nat. Phys. **14**, 213 (2018).

[12] M. Seeman, D. Ködderitzsch, S. Wimmer, and H. Ebert, Symmetry-imposed shape of linear response tensors, Phys. Rev. B **92**, 155138 (2015).

[13] M. T. Suzuki, T. Koretsune, M. Ochi, and R. Arita, Cluster multipole theory for anomalous Hall effect in antiferromagnets, Phys. Rev. B **95**, 094406 (2017).

[14] T. He, Q. Huang, A. P. Ramirez, Y. Wang, K. A. Regan, N. Rogado, M. A. Hayward, M. K. Haas, J. S. Slusky, K. Inumara, H. W. Zandbergen, N. P. Ong, and R. J. Cava, Superconductivity in the non-oxide perovskite MgCNi$_3$, Nature (London) **411**, 54 (2001).

[15] K. Kamishima, T. Goto, H. Nakagawa, N. Miura, M. Ohashi, N. Mori, T. Sasaki, and T. Kanomata, Giant magnetoresistance in the intermetallic compound Mn$_3$GaC, Phys. Rev. B **63**, 024426 (2000).

[16] D. Fruchart and E. F. Bertaut, Magnetic studies of the metallic perovskite-type compounds of manganese, J. Phys. Soc. Jpn. **44**, 781 (1978).

[17] T. Kaneko, T. Kanomata, and K. Shirakawa, Pressure effect on the magnetic transition temperatures in the intermetallic compounds Mn$_3$MC (M = Ga, Zn and Sn), J. Phys. Soc. Jpn. **56**, 4047 (1987).

[18] K. Takenaka, M. Ichigo, T. Hamada, A. Ozawa, T. Shibayama, T. Inagaki, and K. Asano, Magnetovolume effects in manganese nitrides with antiperovskite structure, Sci. Technol. Adv. Mater. **15**, 015009 (2014).

[19] T. Tohei, H. Wada, and T. Kanomata, Negative magnetocaloric effect at the antiferromagnetic to ferromagnetic transition of Mn$_3$GaC, J. Appl. Phys. **94**, 1800 (2003).

[20] B. S. Wang, P. Tong, Y. P. Sun, X. Luo, X. B. Zhu, G. Li, X. D. Zhu, S. B. Zhang, Z. R. Yang, and W. H. Song, Large magnetic entropy change near room temperature in antiperovskite SnCMn$_3$, Europhys. Lett. **85**. 47004 (2009).

[21] D. Matsunami, A. Fujita, K. Takenaka, and M. Kano, Giant barocaloric effect enhanced by the frustration of the antiferromagnetic phase in Mn$_3$GaN, Nat. Mater. **14**, 73 (2015).

[22] E. F. Bertaut, D. Fruchart, J. P. Bouchaud, and R. Fruchart, Diffraction neutronique de MnGaN, Solid State Commun. **6**, 251 (1968).

[23] K. Shi, Y. Sun, J. Yan, S. Deng, L. Wang, H. Wu, P. Hu, H. Lu, M. I. Malik, Q. Huang, and C. Wang, Baromagnetic effect in antiperovskite Mn$_3$Ga$_{0.95}$N$_{0.94}$ by neutron powder diffraction analysis, Adv. Mater. **28**, 3761 (2016).

[24] K. Takenaka, T. Inagaki, and H. Takagi, Conversion of magnetic structure by slight dopants in geometrically frustrated antiperovskite Mn$_3$GaN, Appl. Phys. Lett. **95**, 132508 (2009).

[25] S. Likubo, K. Kodama, K. Takenaka, H. Takagi, and S. Shamoto, Magnetovolume effect in Mn$_3$Cu$_{1-x}$Ge$_x$N related to the magnetic structure: Neutron powder diffraction measurements, Phys. Rev. B **77**, 020409 (2008).

[26] H. Fujita, Field-free, spin-current control of magnetization in non-collinear chiral antiferromagnets, Phys. Status Solidi RRL **11**, 1600360 (2017).

[27] M. Gradhand, D. V. Fedorov, F. Pientka, P. Zahn, I. Mertig, and B. L. Györffy, First-principle calculations of the Berry curvature of Bloch states for charge and spin transport of electrons, J. Phys.: Condens. Matter **24**, 213202 (2012).

[28] D. Vanderbilt, Soft self-consistent pseudopotentials in a generalized eigenvalue formalism, Phys. Rev. B **41**, 7892 (1990).

[29] P. Giannozzi et al., QUANTUM ESPRESSO: A modular and open-source software project for quantum simulations of materials, J. Phys.: Condens. Matter **21**, 395502 (2009).

[30] J. P. Perdew, K. Burke, and M. Ernzerhof, Generalized Gradient Approximation Made Simple, Phys. Rev. Lett. **77**, 3865 (1996).

[31] F. D. Murnaghan, The compressibility of media under extreme pressures, Proc. Natl. Acad. Sci. USA **30**, 244 (1944).

[32] M. B. Nardelli, F. T. Cerasoli, M. Costa, S. Curtarolo, R. De Gennaro, M. Fornari, L. Liyanage, A. Supka, and H. Wang, PAOFLOW: A utility to construct and operate on *ab-initio* Hamiltonians from the projections of electronic wavefunctions on atomic orbital bases, including characterization of topological materials, Comput. Mater. Sci. **143**, 462 (2017).

[33] L. A. Agapito, A. Ferretti, A. Calzolari, S. Curtarolo, and M. B. Nardelli, Effective and accurate representation of extended Bloch states on finite Hilbert spaces, Phys. Rev. B **88**, 165127 (2013).

[34] L. A. Agapito, S. Ismail-Beigi, S. Curtarolo, M. Fornari, and M. B. Nardelli, Accurate tight-binding Hamiltonian matrices from *ab-initio* calculations: Minimal basis sets, Phys. Rev. B **93**, 035104 (2016).

[35] J. Železný, https://www.bitbucket.org/zeleznyj/linear.

[36] K. Momma, and F. Izumi, VESTA: A three-dimensional visualization system for electronic and structural analysis, J. Appl. Crystal. **41**, 653 (2008).

[37] T. Williams, C. Kelley, H. B. Broker, J. Campbell, R. Cunningham, D. Denholm, E. Elber, R. Fearick, C. Grammes, and L. Hart, Gnuplot 4.5: An interactive plotting program, 2011, http://www.gnuplot.

[38] P. Lukashev, R. F. Sabirianov, and K. Belashchenko, Theory of piezomagnetic effect in Mn-based antiperovskites, Phys. Rev. B **78**, 184414 (2008).

[39] J. Zemen, Z. Gercsi, and K. G. Sandeman, Piezomagnetism as a counterpart of the magnetovolume effect in magnetically frustrated Mn-based antiperovskite nitrides, Phys. Rev. B **96**, 024451 (2017).

[40] D.-F. Shao, G. Gurung, T. R. Paudel, and E. Y. Tsymbal, Electrically reversible magnetization at the antiperovskite/perovskite interface, Phys. Rev. Materials **3**, 024405 (2019).

[41] Y. Yao, L. Kleinman, A. H. MacDonald, J. Sinova, T. Jungwirth, D. Wang, and Q. Niu, First-Principles Calculation of Anomalous Hall Conductivity in Ferromagnetic bcc Fe, Phys. Rev. Lett. **92**, 037204 (2004).

[42] D. Boldrin, I. Samathrakis, J. Zemen, A. Mihai, B. Zou, B. Esser, D. McComb, P. Petrov, H. Zhang, and L. F. Cohen, The anomalous Hall effect in non-collinear antiferromagnetic Mn_3NiN thin films, arXiv:1902.04357 (2019).

[43] D. Boldrin, A. P. Mihai, B. Zou, J. Zemen, R. Thompson, E. Ware, B. V. Neamtu, L. Ghivelder, B. Esser, D. W. McComb, P. Petrov, and L. F. Cohen, Giant piezomagnetism in Mn_3NiN, ACS Appl. Mater. Interfaces **10**, 18863 (2018).

[44] C. X. Quintela, K. Song, D.-F. Shao, L. Xie, T. R. Paudel, N. Campbell, M. S. Rzchowski, E. Y. Tsymbal, S.-Y. Choi, and C. B. Eom, Epitaxial antiperovskite/perovskite heterostructures for materials design (unpublished).

[45] X. Zhou, J.-P. Hanke, W. Feng, F. Li, G.-Y. Guo, Y. Yao, S. Blügel, and Y. Mokrousov, Spin-order dependent anomalous Hall effect and magneto-optical effect in the noncollinear antiferromagnets Mn_3XN with X = Ga, Zn, Ag, or Ni, Phys. Rev. B **99**, 104428 (2019).